ORP1L regulates dynein clustering on endolysosmal membranes in response to cholesterol levels

Shreyasi Thakur[1], Peter K. Relich[1], Elena M. Sorokina[1], Melina T. Gyparaki[2], Melike Lakadamyali[1,3,*]

[1] Department of Physiology, Perelman School of Medicine, University of Pennsylvania

[2] Department of Biology, School of Arts and Sciences, University of Pennsylvania

[3] Department of Cell and Developmental Biology, Perelman School of Medicine, University of Pennsylvania

[*] Correspondence should be sent to: melikel@pennmedicine.upenn.edu

Abstract

The sub-cellular positioning of endolysosomes is crucial for regulating their function. Particularly, the positioning of endolysosomes between two sub-cellular locations – the cell periphery versus the peri-nuclear region – impacts autophagy, mTOR (mechanistic target of rapamycin) signaling and other processes. The mechanisms that regulate the positioning of endolysosomes at these two locations are still being uncovered. Here, using quantitative super-resolution microscopy, we show that the retrograde motor dynein forms nano-clusters on endolysosomal membranes containing 1-4 dynein motors. Surprisingly, dynein nano-clusters are larger on peripherally positioned endolysosomes having higher cholesterol levels compared to peri-nuclear ones. By perturbing endolysosomal membrane cholesterol levels, we show that dynein copy number within nano-clusters directly depends on the amount of endolysosomal cholesterol. Finally, we show that the dynein adapter protein ORP1L (Oxysterol Binding Protein Homologue) increases dynein clustering in response to increased membrane cholesterol levels. Our work reveals a new mechanism by which endolysosomal positioning is regulated through the cholesterol dependent nano-organization of ORP1L and dynein.

Introduction

Late endosomes, lysosomes and autolysosomes constitute a broad class of sub-cellular compartments (Klumperman and Raposo, 2014; Wijdeven et al., 2016) that we will refer to here as endolysosomes for simplicity. These compartments play key cellular roles including transport of cellular proteins destined for degradation, metabolic sensing, membrane repair and signaling (Gould and Lippincott-Schwartz, 2009). The maturation level, fusion capacity with other sub-cellular compartments and downstream function of endolysosomes are regulated by their intracellular transport and sub-cellular positioning. For example, dispersal of lysosomes from the peri-nuclear region to the cell periphery increases their association with mTORC1 (mechanistic target of rapamycin complex 1) and leads to downregulation of autophagy (Kimura et al., 2008; Korolchuk and Rubinsztein, 2011; Korolchuk et al., 2011; Pu et al., 2016). The transport and subcellular positioning of endolysosomes are in turn regulated by a myriad of mechanisms(Maday et al., 2014) including motor activation (Elshenawy et al., 2020; Fu and Holzbaur, 2014; Fu et al., 2014), motor tug-of-war (Belyy et al., 2016; Hendricks et al., 2010; Soppina et al., 2009) and association of motors with microtubule tracks having distinct post-translational modifications (Guardia et al., 2016; Mohan et al., 2019; Nirschl et al., 2016).

Peripheral transport of endolysosomes is mediated by kinesin motors belonging to different kinesin families (Kif5, Kif1, Kif3) (Brown et al., 2005; Cardoso et al., 2009; Encalada et al., 2011; Mohan et al., 2019; Rosa-Ferreira and Munro, 2011), whereas dynein is responsible for their retrograde transport toward the perinuclear region (Granger et al., 2014; Reck-Peterson et al., 2018). Recent discovery of dynein activating adapters have revolutionized our understanding of how dynein mediates efficient retrograde transport (Elshenawy et al., 2020; McKenney et al., 2014; Olenick and Holzbaur, 2019; Reck-Peterson et al., 2018; Schroeder and Vale, 2016). Dynein assembles into an autoinhibitory, weakly processive conformation, while dynein activating adaptors are crucial for dynein's assembly with dynactin and the processive motility of the dynein-dynactin complex on microtubules (Chowdhury et al., 2015; McKenney et al., 2014; Schroeder and Vale, 2016; Urnavicius et al., 2018). Recent Cryo-EM studies showed that certain early endosomal dynein activating adapters including BICD2 and Hook3 recruit two dynein dimers (Urnavicius et al., 2018). *In vitro* assays further showed that these heteromeric dynein complexes move faster and navigate obstacles better compared to single dynein (Elshenawy et al., 2019; Ferro et al., 2019; Urnavicius et al., 2018). Hence, in addition to mediating dynein's interaction with dynactin and bringing dynein out of its auto-inhibitory confirmation, these activators further

improve the efficiency of dynein mediated motility by allowing two copies of dynein to assemble together into complexes. Yet, to date, the stoichiometry of adapter-dynein-dynactin complexes on sub-cellular compartments i*n vivo* and how these complexes are spatially organized on the membrane of sub-cellular compartments are not known. Dynein is recruited to endolysosomal compartments via the cholesterol-sensing tripartite complex Rab7-RILP-ORP1L (Johansson et al., 2007; Pfeffer, 2001; Rocha et al., 2009). Whether this tripartite complex can recruit multiple copies of dynein dimers to improve the efficiency of retrograde transport of endolysosomal compartments in response to cellular cues is unknown.

Super-resolution is a powerful tool for studying spatial nano-organization of proteins within the cell, yet, only a handful of studies have been carried out to date to visualize proteins on the membrane of sub-cellular compartments (Franke et al., 2019; Puchner et al., 2013). Previously, using super-resolution microscopy, we showed that dynein forms nano-clusters on microtubules consisting of small teams of dynein motors (Cella Zanacchi et al., 2019; Zanacchi et al., 2017a). However, whether these nano-clusters are formed on the membrane of endolysosomes, the mechanisms of nano-cluster formation and whether formation of larger nano-clusters containing more dynein motors lead to more efficient retrograde transport are not known. Here, using quantitative super-resolution microscopy, we show that dynein forms nano-clusters on endolysosomes, consisting of 1-4 dyneins. Our data suggest that for efficient retrograde transport, dynein should be present in multiples of two copies within nano-clusters (e.g. 4 dyneins). The copy number of dynein within nano-clusters is in turn regulated by membrane cholesterol levels and ORP1-L's cholesterol sensing domain.

Results

Dynein forms nano-clusters on endolysosomes containing 1-4 dynein motors with a switch to larger nano-clusters on peripheral versus peri-nuclear endolysosomes.

To visualize the spatial organization of dynein on endolysosomal membranes we expressed mCherry-ORP1L in HeLa cells in which endogenous ORP1L was targeted by CRISPR/Cas9 mutagenesis (ORP1L-KO)(Zhao and Ridgway, 2017). The mCherry-ORP1L signal substantially overlapped with that of CD63, an endolysosomal marker (Beatty, 2006; van der Kant et al., 2013; Vanlandingham and Ceresa, 2009), indicating that ORP1L marks endolysosomes (Figure S1A). Hence, we took mCherry-ORP1L positive sub-compartments in the wide-field images that were isolated, round and diffraction limited in size (200-500 nm FWHM) as an endolysosome for further

analysis (Figure 1A and S1B). To determine whether dynein was clustered on these endolysosomes, we carried out super-resolution imaging of dynein labeled with an antibody against the dynein intermediate chain (IC74). These images revealed nano-clusters within the cell cytoplasm similar to what we have previously demonstrated (Cella Zanacchi et al., 2019) (Figure 1A-B). We manually cropped the central intensity peak of mCherry-ORP1L positive endolysosomes (Figure S1B and Methods) and used it as a mask in the super-resolution image to specifically segment dynein nano-clusters that overlapped with an endolysosomal compartment (Figure 1A-B). Dynein super-resolution images were further segmented into individual nano-clusters using a previously developed Voronoi tessellation approach (Figure S1C) (Levet et al., 2015). We then quantified the number of localizations per dynein nano-cluster for peripherally- and peri-nuclearly-positioned endolysosomes (Figure 1C). The peripheral and peri-nuclear endolysosomes were separated manually based on their proximity to the cell nucleus (Figure S1D). The number of localizations per nano-cluster is proportional to the nano-cluster size as well as to the copy number of dynein within nano-clusters (Cella Zanacchi et al., 2019; Zanacchi et al., 2017a). Surprisingly, we found that the dynein nano-clusters associated to peripheral endolysosomes contained a significantly higher number of localizations compared to peri-nuclear endolysosomes (mean = 53±1.8 for peripheral and 65±1.8 for perinuclear endolysosomes) (Figure 1C). To obtain a quantitative estimate of the copy number of dynein within nano-clusters, we carried out a calibration experiment in which we diluted the primary antibody by 100-fold, aiming to sparsely label single copies of dynein (Ehmann et al., 2014) (Methods, Figure S1E). We then used the number of localizations per dynein nano-cluster in these sparse labeling experiments as a calibration corresponding to single dynein motor (Figure 1C, Figure S1F). We previously showed that fitting the distribution of number of localizations per nano-cluster to a linear convolution of monomeric calibration functions enables estimation of the copy number composition of a protein of interest in super-resolution images (Zanacchi et al., 2017b), Using this approach, we estimated that nano-clusters on peri-nuclear endolysosomes mainly consist of 1-2 copies of dynein motor (74% single, 11% 2, 7% 3 and 8% 4 copies) (Figure S1F). Interestingly, on peripheral endolysosomes the proportion of nano-clusters containing 1-2 dynein motors decreased and the proportion of nano-clusters containing 3-4 motors increased (70% single, 2% 2, 9% 3 and 18% 4 copies of dynein (Figure S1F). In particular, there was a 2-fold increase in the proportion of nano-clusters with 4 copies of dynein on peripheral endolysosomes. We next asked if the membrane cholesterol content may be responsible for increased dynein clustering and the switch from primarily 1-2 copies of dynein to increased 3-4 copies of dynein on peripheral endolysosomes. To start addressing this question, we measured

the cholesterol levels of peripheral and peri-nuclear endolysosomes by labeling mCherry-ORP1L expressing HeLa cells with filipin, a toxin that binds cholesterol. We measured the filipin intensity on mCherry-ORP1L positive endolysosomes and found that membrane cholesterol levels of peripheral endolysosomes were indeed higher compared to peri-nculear endolysosomes (Figure 1D). These results indicate a correlation between endolysosomal membrane cholesterol levels, endolysosomal positioning and dynein clustering.

Membrane cholesterol levels determine the level of dynein clustering and dynein copy number within nano-clusters on endolysosomes.

It is known that positioning of endolysosomal compartments in the cell affects their membrane composition, maturation and signaling (Cabukusta and Neefjes, 2018; Hu et al., 2015; Hyttinen et al., 2013). To better understand the mechanisms behind dynein clustering and to causally relate dynein clustering to endolysosomal membrane cholesterol levels, we manipulated cholesterol levels with two commonly used drugs: U18666A that increases endolysosomal membrane cholesterol and Lovastatin that decreases cellular and endolysosomal membrane cholesterol levels (Keyomarsi, 1996; Rocha et al., 2009). mCherry-ORP1L-positive endolysosomes in ORP1L KO HeLa cells treated with U18666A indeed had higher membrane cholesterol levels (by 4.5-fold) compared to those in cells treated with lovastatin as measured by filipin intensity (Figure S2A). We will refer to the endolysosomal membrane cholesterol content of the U18666A and Lovastatin treated cells as ‘high cholesterol’ and ‘low cholesterol’ condition, respectively.

Super-resolution imaging revealed that dynein nano-clusters on endolysosomal compartments contained a significantly higher number of localizations under high cholesterol compared to low cholesterol conditions (mean = 71±1.9 for high and 50±1.9 for low cholesterol) (Figure 2A-B). These differences were not due to an increase in dynein expression level upon high cholesterol drug treatment, as western blot analysis showed that the level of dynein expression did not increase under high cholesterol treatment (Figure S2B). We fit the number of localizations per nano-cluster distribution to the calibration data to determine dynein copy number within nano-clusters under high and low cholesterol conditions (Figure S2C). This analysis showed that dynein nano-clusters change from containing mainly single dynein motors to containing an increased proportion of dynein multimers (75% single, 9% 2, 13% 3 and 3% 4 copies of dynein under low cholesterol conditions and 58% single, 13% 2, 1.2% 3 and 27% 4 copies of dynein under high cholesterol conditions) (Figure S2C). Interestingly, there was a dramatic increase in the proportion

of nano-clusters containing 4 copies of dynein (9-fold) similar to the observations for peripheral versus peri-nuclear endolysosomes. Finally, low cholesterol levels also led to an increase in the percentage of endolysosomes that completely lacked dynein (Figure S2D).

We next analyzed the cholesterol levels of and dynein nano-cluster size on peripheral and peri-nuclear endolysosomes under the two cholesterol treatment conditions. In contrast to physiological conditions, peripheral and peri-nuclear endolysosomes had similar cholesterol levels (Figure S2E) and similar dynein clustering (Figure 2C) under both high and low cholesterol conditions. Interestingly, the dynein clustering level of peri-nuclear endolysosomes under physiological conditions was similar to those under low cholesterol conditions and the dynein clustering level of peripheral endolysosomes under physiological conditions was similar to those under high cholesterol conditions (Figure 2D). These results indicate that cholesterol levels and not endolysosome positioning determine the level of dynein clustering on endolysosomal membranes. Finally, the positioning of endolysosomes were impacted by cholesterol levels, with low cholesterol leading to more scattered and high cholesterol leading to more peri-nuclearly positioned endolysosomes (Figure S2F), consistent with previous results (Rocha et al., 2009).

Taken together our results show that membrane cholesterol levels impact not only dynein recruitment but importantly also the level of dynein clustering and the proportion of dynein multimers on endolysosomal membranes, impacting the balance between antero- and retro-grade transport of these compartments and leading to their re-positioning with respect to the cell peri-nuclear region.

The cholesterol sensing domain of ORP1L regulates ORP1L clustering on endolysosomal membranes in a cholesterol dependent manner.

Dynein does not bind directly to endolysosomal membranes and the mechanisms that can lead to the formation of larger dynein nano-clusters with increased number of dynein motors in them are unknown. Dynein is recruited to endolysosomes through a tripartite complex of Rab7-ORP1L-RILP (Johansson et al., 2007; Pfeffer, 2001; Rocha et al., 2009). ORP1L contains multiple lipid binding domains that allow it to bind to either oxysterols or phospholipids (Johansson et al., 2005; Olkkonen and Li, 2013; Zhao and Ridgway, 2017). Hence, we asked whether the cholesterol sensing domain of ORP1L is responsible for regulating dynein clustering on endolysosomal membranes. To address this question, we first imaged ORP1L's spatial distribution on endolysosomes in wild type or ORP1L-KO HeLa cells that express mCherry-ORP1L (Zhao and

Ridgway, 2017) under low or high cholesterol treatment conditions using super-resolution microscopy (Figure 3A). We again analyzed isolated, round mCherry-ORP1L positive endolysosomes within a size range of 50-500 nm in the super-resolution images. ORP1L appeared uniformly distributed on the endolysosomal membrane under low cholesterol conditions and more clustered under high cholesterol conditions (Figure 3A). To quantify the level of ORP1L clustering, we once again used Voronoi tessellation to segment individual ORP1L clusters on endolysosomal membranes. This approach revealed an increased number of ORP1L clusters under high cholesterol (Mean: 2.6) compared to low cholesterol (Mean: 1) conditions (Figure S3A). However, we also found that, surprisingly, the localization density of ORP1L was higher on endolysosomes under low cholesterol compared to high cholesterol conditions (Figure S3B), suggesting that more ORP1L binds to endolysosomes when their membrane cholesterol levels are lower. To ensure that the increased protein density does not confound the clustering analysis using Voronoi tessellation, which is dependent on localization density, we developed an alternative quantification method that is insensitive to differences in localization density and protein amount (Methods). To this end, we carried out Voronoi tessellation and re-scaled the distribution of Voronoi polygon areas so that the mean area was set to unity. We refer to the re-scaled quantities as reduced areas. The distribution of reduced areas provides a means to measure the clustering tendency of ORP1L from various conditions without explicitly compensating for different localization densities. For a clustered distribution, we expected to see a shift in the mode of the reduced Voronoi polygon area distribution towards a smaller value. Indeed, the mode of the distribution for endolysosomal compartments under high cholesterol conditions was shifted to smaller polygon areas compared to low cholesterol conditions or compared to a simulated random distribution, indicating that ORP1L is more clustered on endolysosomes with high membrane cholesterol levels (Figure 3B). We further used a statistical test (Kullback-Leibler Divergence or KL Divergence) to determine how much ORP1L organization differed from a random distribution under low and high cholesterol conditions. The difference from the normalized random distribution of points to the experimental distribution, which we call the clustering tendency score, was 0.75 under high cholesterol and 0.14 under low cholesterol (a 5-fold difference). These results further confirm that ORP1L's organization on endolysosomal membranes deviated significantly more from a random distribution under high cholesterol compared to low cholesterol conditions. When endogenous ORP1L on CD63 positive endolysosomal compartments was imaged in wild type HeLa cells using an ORP1L antibody, it also was more clustered and had lower localization density under high cholesterol compared to low cholesterol conditions (Figure S3C-D), demonstrating that the results are not an artifact of

ORP1L over-expression. Overall, these super-resolution data show that ORP1L, like dynein, is more clustered on endolysosomes having higher membrane cholesterol levels.

To determine if the differences in ORP1L's spatial distribution on endolysosomes were due to its cholesterol binding, we expressed mCherry fused to a sterol binding deficient ORP1L mutant lacking the residues 560–563 (mCherry-ORP1L-SBD) (Vihervaara et al., 2011; Zhao and Ridgway, 2017) in HeLa ORP1L KO cells (Figure 3C-D and Figure S3E-F). Super-resolution images of the mCherry-ORP1L-SBD mutant (Figure 3C) and both Voronoi cluster segmentation (Figure S3E) and reduced Voronoi polygon area distribution analysis (Figure 3D) (Clustering tendency score for ORP1L-SBD: 0.1 for high and 0.09 for low cholesterol conditions) showed that the distribution of the ORP1L-SBD mutant was uniform on endolysosomal membranes independent of cholesterol levels. The membrane localization density of this mutant was overall high under both high and low cholesterol conditions (Figure S3F) and at a similar level to the full length ORP1L under low cholesterol conditions (Figure S3B). These results suggest that under low cholesterol or when ORP1L lacks its cholesterol sensing domain, it is recruited to and binds phospholipids on endolysosomes at a high level and likely in a non-specific manner. Finally, under physiological conditions (no cholesterol treatment) the full-length ORP1L was more clustered on peripherally positioned endolysosomes that have higher cholesterol levels whereas these differences in ORP1L clustering were absent for the ORP1L-SBD mutant (Figure S4A-B).

Overall, these results strongly support that the cholesterol sensing domain of ORP1L regulates its spatial distribution on endolysosomal membranes in a cholesterol dependent manner, with high cholesterol leading to more specific ORP1L recruitment (Figure S3B) and a clustered ORP1L spatial organization (Figure 3A-B).

The cholesterol sensing domain of ORP1L regulates dynein clustering and endolysosomal positioning in a cholesterol dependent manner.

Having established that ORP1L's cholesterol sensing domain regulates ORP1L's level of clustering on endolysosomal membranes in a cholesterol dependent manner, we next asked if ORP1L's spatial organization also impacts dynein clustering. We thus imaged dynein using super-resolution microscopy in ORP1L-KO HeLa cells expressing the mCherry-ORP1L-SBD mutant. Analysis of dynein nano-clusters on endolysosomes under high and low cholesterol conditions showed that dynein clustering was no longer sensitive to cholesterol levels in cells expressing the mCherry-ORP1L-SBD mutant as the sole ORP1L isoform (mean = 51±1.2 for high and 53±.88 for

low cholesterol) (Figure 4A-B). In addition, the level of dynein clustering in cells expressing the mCherry-ORP1L-SBD mutant was similar to the level of dynein clustering under low cholesterol conditions in cells expressing the full length mCherry-ORP1L (compare Figure 2B and Figure 4B).

The sub-cellular positioning of endolysosomes also became insensitive to cholesterol treatment in cells expressing the mCherry-ORP1L-SBD mutant and the endolysosomes were overall more scattered throughout the cell under high or low cholesterol conditions as well as under physiological conditions (Figure S4C). Finally, peripheral and peri-nuclear endolysosomes had similar level of dynein clustering in untreated cells expressing the mCherry-ORP1L-SBD mutant (mean = 71±6 for high and 66±2 for low cholesterol) (Figure 4C). Taken together, these results show that the increased clustering and higher copy number of dynein within nano-clusters on peripherally located endolysosomes with higher cholesterol content is dependent on the cholesterol binding and clustering ability of ORP1L (Figure 4D).

Discussion

Here using super resolution microscopy and quantitative analysis, we visualize the spatial organization of dynein motor and its adapter protein ORP1L on endolysosomal membranes. We find that dynein forms nano-clusters consisting of mainly single but also a small but significant proportion of multiple copies of dynein motor. Using perturbation experiments in which we manipulated endolysosomal membrane cholesterol levels we show that the level of dynein clustering and the copy number of dynein within nano-clusters on endolysosomal membrane is increased under high cholesterol. This increased clustering is regulated by the cholesterol binding ability of ORP1L that forms part of the Rab7-ORP1L-RILP tripartite complex, which recruits dynein to endolysosomal membranes.

Cryo-EM experiments demonstrated that BICD2 and Hook3 bind two copies of dynein motors (Urnavicius et al., 2018) but whether the endolysosomal adapter proteins Rab7-ORP1L-RILP also recruit multiple dyneins is unknown. Our results demonstrate that besides the stoichiometry between motor proteins and their adapter proteins, additional mechanisms inside cells are at play to increase motor protein clustering and retrograde transport efficiency. We show that clustering of adapter proteins into cholesterol enriched domains impacts the clustering of dynein motor on endolysosomal membranes, increasing the efficiency of retrograde transport. High cholesterol treatment increased the proportion of nano-clusters containing dynein multimers, with a big increase on the proportion of nano-clusters containing 4 copies of dynein. Peripheral

endolysosomes also had a higher proportion of nano-clusters with 4 copies of dynein compared to perinuclear endolysosomes. These results suggest that having dynein present in multiple copies of two may be important for efficient retrograde transport, which is consistent with the recent Cryo-EM and in vitro single molecule imaging data showing that coupled dyneins move more processively and faster than single dynein (Urnavicius et al., 2018).

Previous *in vitro* work showed that early phagosomes engulfing 2-micron sized polystyrene beads isolated from dictyostelium cells were completely uniformly covered with dynein on their membrane whereas late phagosomes that move unidirectionally towards the retrograde direction had a highly clustered dynein distribution (Rai et al., 2016). These changes in dynein distribution were correlated to the membrane cholesterol content of phagosomes. In contrast, our results show that instead of uniformly covering the entire membrane, only a small number of dyneins are associated to endolysosomal membranes *in vivo.* A dramatic shift from a uniform dynein coverage to a highly clustered dynein distribution hence is not needed for regulating retrograde transport of native cellular compartments as these previous experiments with non-native compartments suggested. Instead, a small shift from mainly single copies of dynein to a small proportion of dynein mutimers (in particular containing 4 dyneins) is sufficient to bias retrograde transport of native sub-cellular compartments.

Interestingly, the number of dyneins within nano-clusters is higher for peripherally located endolysosomes, which also have higher cholesterol levels. Endolysosomes contact the endoplasmic reticulum as they are trafficked within the cell cytoplasm (Friedman et al., 2013; Rocha et al., 2009; Zhao and Ridgway, 2017). Such contacts lead to exchange of membrane lipids and maturation of endolysosomes (van der Kant et al., 2013; Zhao and Ridgway, 2017). It is plausible that multiple endolysosome-ER contacts during retrograde transport play a role in lowering the cholesterol content of endolysosomes, leading to re-organization of ORP1L and decreased dynein clustering. Hence, the peripheral endolysosomes with higher level of dynein clustering are potentially those that are on their way to be retrogradely transported. Future correlative live-cell and super-resolution imaging experiments (Balint et al., 2013; Mohan et al., 2019; Verdeny-Vilanova et al., 2017) will enable directly linking the transport properties of endolysosomes to the level of dynein clustering on their membrane. Loss of membrane cholesterol through ER contacts as these endolysosomes are retrogradely transported potentially leads to loss of dynein clustering facilitating stalling/positioning at the perinuclear region or anterograde trafficking back to the cell periphery via kinesin.

Previous studies showed that ORP1L, depending on its conformation, can either bind dynein or make contacts with the ER-membrane (Olkkonen and Li, 2013; Rocha et al., 2009; Wijdeven et al., 2016; Zhao and Ridgway, 2017). A change in ORP1L's conformation leads to shedding of dynein and initiation of contact between ORP1L and the ER-membrane protein VAP to regulate endolysosomal positioning (Rocha et al., 2009). Our results are consistent with these former studies as we show that in addition to the level of dynein clustering, the recruitment of dynein to endolysosomal compartments is also dependent on cholesterol levels. Under low cholesterol, the percentage of endolysosomes completely lacking dynein was increased by ~2-fold (from 27% to 55%). However, around 45% of endolysosomes still contained dynein on their membrane even under low cholesterol conditions. Here, we additionally show that ORP1L's nanoscale spatial organization on the endolysosomal membranes is also dependent on cholesterol levels and regulates dynein clustering, not only dynein recruitment. Hence, multiple mechanisms, including recruitment of more dynein motors and clustering of the recruited dynein motors on the endolysosomal membrane, are at play to increase the efficiency of retrograde transport and regulate endolysosomal positioning. It will be interesting in the future to examine the differential impact of having more dynein versus having dynein clustered in copies of two on the transport and positioning of endolysosomes. It is plausible to hypothesize that increased dynein recruitment in the absence of dynein clustering is not sufficient for enhancing retrograde transport.

Overall, our results provide an *in vivo* mechanism dependent on cholesterol levels by which multiple dyneins can be recruited and clustered on endolysosomal membranes leading to their efficient retrograde transport and positioning. Increased dynein clustering in response to cholesterol levels is likely to be functionally significant as it impacts the sub-cellular positioning of endolysosomal compartments. Metabolic disorders that lead to accumulation of lipids including cholesterol in endolysosomal compartments like Niemann Pick Disease (NPC) are typically associated with alterations in endolysosomal homeostasis and function (Torres et al., 2017). In the future it would be interesting to explore if the nanoscale organization of ORP1L and dynein is altered on endolysosomal membranes in NPC and other lysosomal storage disorders leading to their mislocalization within the cell and whether restoring the proper nanoscale organization of these cytoskeletal proteins can restore endolysosomal function. It would also be interesting to determine if similar mechanisms play a role in regulating kinesin clustering or in regulating transport of other organelles including Golgi vesicles and autophagosomes. It would further be exciting to determine the precise stoichiometry of adapter-motor complexes on organelle membranes to determine how the stoichiometry can be precisely tuned to regulate organelle

transport and positioning. Our work establishes the methodology needed and opens the door to carry out these future studies.

Materials and Methods

Cells and transfections

Wild type HeLa cells were obtained from the American Type Culture Collection (CCL-2, ATCC, Manassas, VA). HeLa-ORP1L-null cell lines, as well as mCherry-tagged ORP1L and ORP1L-SBD constructs were a kind gift from Prof. Neale Ridgway (Dalhousie University, Depts. of Pediatrics, and Biochemistry and Molecular Biology, Atlantic Research Centre, Halifax, Nova Scotia, Canada). HeLa cells were grown in DMEM (GIBCO Laboratories, Grand Island, NY) supplemented with 10% fetal bovine serum and antibiotics, and maintained in 5% CO2 at 37°C. Cells were transiently transfected with mCherry-tagged wild type or mutant ORP1L at 70% confluency using Lipofectamine 2000 reagent (Invitrogen) according to the manufacturer's protocol. Cells were subjected to experimental treatments 24 h after transfection.

Pharmacological treatment of cells

Lovastatin (Sigma 1370600) was converted from its inactive prodrug form to its active open acid form by dissolving Lovastatin (52gms) in ethanol (95%, 1.04 ml), followed by addition of 1N NaOH (813 µl), followed by heating for 2 hrs at 50°C and neutralized with 1N HCL (pH 7.2). The volume was made up to 13 ml by adding distilled water, giving 10mM active Lovastatin solution later aliquoted and stored at -20°C(Keyomarsi, 1996). Mevalonic acid lactone (Sigma M4667, 1 gm) was converted to its active form by dissolving in ethanol (3.5 ml), followed by addition of 1N NaOH (4.2 ml) and heating for 2 hrs at 55°C. The solution was made up to 15.4 ml with distilled water and neutralized with 1N HCL (pH 7.2), giving 500 mM of stock solution, later aliquoted and stored at -20. U18666A (Sigma U3633) was dissolved in ethanol giving final concentration of 10mg/ml(Rocha et al., 2009). For cholesterol depletion treatment, cells were cultured in DMEM, 10% Lipoprotein deficient serum (Sigma S5394), 50uM Lovastatin, 230uM Mevalonate for 6 hrs before fixing for immunostaining. For high cholesterol treatment cells were cultured in DMEM, 10% FBS and 3µg/ml U18666A for 12 hrs before fixing.

Immunostating

Hela ORP1L KO cells were transiently transfected with ORP1L WT-mCherry or ORP1L SBD-mCherry, treated with U18666A/Lovastatin or not treated and immunostained for ORP1L and

dynein. Endogenous ORP1L was immunostained in untransfected Hela cells treated with U18666A/Lovastatin or not treated. For ORP1LWT/SBD-mCherry and endogenous ORP1L immunostaning, cells were fixed with 4% (Vol/Vol) Paraformaldehyde in PBS for 20 mins and for dynein immunostaining, cells were fixed in prechilled 1:1 Ethanol/Methanol solution for 3 mins on ice. The cells were blocked in blocking buffer (3% BSA, 0.2% Triton X-100 in PBS) for 1 hr. Cells were incubated with primary anitbodies: Chicken anti-mCherry (Novus biotech nbp2-2515, 1:500) ,mouse anti-dynein (Abcam ab23905, 1:50 or 1:5000 for single dynein imaging) and rabbit anti-ORP1L (Abcam ab131165, 1:100) in blocking buffer for 1 hr on a rocker. Cells were washed with washing buffer (0.2% blocking buffer, .05% Triton X-100 in PBS) three times. Custom made secondary antibodies were labeled with an Alexa Fluor 405–Alexa Fluor A647 activator/reporter dye pair combination at concentrations (0.1-0.15 mg/µl) and used in the ratio of 1:50 in blocking buffer for 40 mins, at RT on a rocker. Sample was then washed three times in PBS.

Filipin staining

Filipin (Sigma F4767) was lyophilized, aliquoted (250 µg per aliquot) and stored at -80°C. Filipin was resuspended in 5 µl DMSO. Cells were fixed in 4% Paraformaldehyde for 20 mins and then rinsed 3 times with PBS. Background autofluorescence was quenched with 50mM NH_4CL for 10 mins. Cells were incubated for 2 hrs with 100 µg/ ml working solution of Filipin in 3% BSA. Cells were washed with 1% BSA in PBS three times before imaging. Imaging was performed immediately.

Western blot

Western blot analysis was performed using the two-color Odyssey LI-COR (Lincoln, NE) technique according to the manufacturer's protocol. A rabbit monoclonal antibody to ORP1L (ab131165, Abcam), mouse monoclonal antibody to dynein (ab23905, Abcam), and a mouse monoclonal antibody to detect GAPDH (clone 3B1E9, GenScript A01622–40) were used at a dilution of 1:1,000 in blocking buffer. The secondary antibody IRDye800CW Donkey anti-Rabbit and IRDye680RD Donkey anti-Mouse (LI-COR) were used in 1:10000 dilution for imaging in the green 800-nm and red 700-nm channels, respectively.

STORM Imaging

Single-molecule imaging was done using imaging buffer comprising of 50 mM Tris, pH 7.5, 10 mM NaCl, 0.5 mg/mL glucose oxidase (Sigma, G2133), 40 µg/mL catalase (Roche Applied Science, 106810), 10% (w/v) glucose and 10% (v/v) Ciseamine (77mg/ml of 360mM HCL) (Bates

et al., 2007). Images were acquired on the Oxford Nanoimager-S microscope which has the following configuration: 405, 488, 561, and 640 nm lasers, 498–551 and 576–620 nm band-pass filters in channel 1, and 665–705 nm band-pass filters in channel 2, 100× 1.4 NA objective (Olympus), and a Hamamatsu Flash 4 V3 sCMOS camera. Localizations were acquired with 10-ms exposure over 50,000 frames with 405 nm activation and 647 nm excitation. Images were processed and localizations were obtained using the NimOS localization software (Oxford Nanoimaging).

Data Analysis

To identify dynein clusters on ORP1L positive compartments, the intensity profile of conventional ORP1L image was used as a mask. Line intensity profile of the ORP1L conventional image along x and y axis was plotted on image J, and the width across one third of the full intensity maxima was considered as the mask (Figure S1B).

For quantitative analysis we used custom written MATLAB codes. A previously described method was adapted that segments super-resolution images based on Voronoi tessellation of the fluorophore localizations (Andronov et al., 2016; Levet et al., 2015). Voronoi tessellation of a STORM image assigns a Voronoi polygon to each localization, such that the polygon area is inversely proportional to the local localization density. The spatial distribution of dynein or ORP1L localizations from each ORP1L positive endolysosome is represented by a set of Voronoi polygons such that smaller polygon areas correspond to regions of higher density. The Voronoi polygons at the endolysosomal edge are extremely large and were omitted for any quantification. Dynein and ORP1L clusters were segmented by grouping adjacent Voronoi polygons with areas less than a selected threshold and imposing a minimum number of localizations. For mCherry-ORP1L, mCherry-ORP1L-SBD, dynein (ORP1L positive endolysosomes) and dynein (ORP1L-SBD positive endolysosomes), the selected area thresholds were 0.0156 px^2, 0.02 px^2, 0.01 px^2 and , 0.01 px^2, respectively and the minimum number of localizations imposed were16,10, 7 and 7, respectively. ORP1L localization density was calculated by normalizing the total number of localizations per endolysosme by endolysosome area. Each endolysosme area was calculated by summing up all of its Voronoi polygon areas. The low cholesterol treatment yielded endolysosomes with ORP1L localization densities 4.5 times higher as compared to the high cholesterol treated endoslysosome localization densities. To compare endoslysomal ORP1L distribution following cholesterol treatments, the ORP1L localization densities should be comparable. To address this we divided the Voronoi polygon areas of each endolysosome by its mean Voronoi polygon area, such that the mean localization density of each endolysosome is in

reduced units of 1. All reduced Voronoi polygon areas from each endolysosme for each treatment were pulled together, and the histogram was plotted. The distribution of Voronoi areas from uniformly simulated random points is fit to an analytical distribution (Tanemura, 2003). A method for calculating the KL divergence between two histograms or between a histogram and an analytical distribution (Perez-Cruz, 2008) was implemented in Matlab. The KL divergence scores between the experimental reduced voronoi areas and the theoretical random distribution were calculated to determine the clustering tendency score of each cholesterol treatment. All ORP1L and dynein analysis has been done with endolysosmes with radius < 250nm for consistency.

For quantification of dynein copy numbers, the single dynein data was fit to a lognormal distribution from which the μ and σ values are obtained. Using these values, the high and low cholesterol dynein data is fit for the sum of convolutions of the single dynein data until a good fit is obtained that does not change with fitting to higher copy number. Here, we fit until 4 dyneins.

Filipin intensity was calculated using Image J 'plot profile' tool. All ORP1L positive endolysosomes were analyzed by drawing a line segment across it and looking at its intensity profile using the 'plot profile' tool. The average of 3-4 highest intensity points were taken and the average background intensity was subtracted from that. For the analysis of dynein clusters on ORP1L positive endolysosmal compartments, a intensity plot of the conventional ORP1L image was taken and all dynein clusters falling within the Full Width Half Maxima of the profile was accepted.

Acknowledgements

We thank Prof. Neale D. Ridgway, Dalhousie University for the Hela cells that are a knockout for ORP1L and for the mCherry-ORP1L and mCherry-ORP1L-SBD constructs. We thank Prof. Michael S. Marks, UPenn, for critical reading and feedback on the manuscript. ML acknowledges funding from the National Institutes of Health/National Institutes for General Medical Sciences (NIH/NIGMS) under the grant numbers: RO1 GM 133842-01 and 1RM1GM136511-01 and the Center for Engineering and Mechanobiology (CEMB) an NSF Science and Technology Center Pilot Award under grant agreement CMMI: 15-48571.

Author Contributions

ML and ST conceived of the study. ST prepared samples, carried out experiments, wrote software and analyzed data. P.K.R. wrote software and implemented the renormalized voronoi area

distribution and KL-Divergence analysis methodology. E.M.S. maintained cell lines, carried out western blot experiments, carried out all transfections, provided reagents and helped with sample preparation. M.T.G. helped carry out dilution and calibration experiments. ML wrote the manuscript, acquired funding and supervised the work. All authors provided feedback on the manuscript.

References

Andronov, L., I. Orlov, Y. Lutz, J.L. Vonesch, and B.P. Klaholz. 2016. ClusterViSu, a method for clustering of protein complexes by Voronoi tessellation in super-resolution microscopy. *Sci Rep*. 6:24084.

Balint, S., I. Verdeny Vilanova, A. Sandoval Alvarez, and M. Lakadamyali. 2013. Correlative live-cell and superresolution microscopy reveals cargo transport dynamics at microtubule intersections. *Proc Natl Acad Sci U S A*. 110:3375-3380.

Bates, M., B. Huang, G.T. Dempsey, and X. Zhuang. 2007. Multicolor super-resolution imaging with photo-switchable fluorescent probes. *Science*. 317:1749-1753.

Beatty, W.L. 2006. Trafficking from CD63-positive late endocytic multivesicular bodies is essential for intracellular development of Chlamydia trachomatis. *J Cell Sci*. 119:350-359.

Belyy, V., M.A. Schlager, H. Foster, A.E. Reimer, A.P. Carter, and A. Yildiz. 2016. The mammalian dynein-dynactin complex is a strong opponent to kinesin in a tug-of-war competition. *Nat Cell Biol*. 18:1018-1024.

Brown, C.L., K.C. Maier, T. Stauber, L.M. Ginkel, L. Wordeman, I. Vernos, and T.A. Schroer. 2005. Kinesin-2 is a motor for late endosomes and lysosomes. *Traffic*. 6:1114-1124.

Cabukusta, B., and J. Neefjes. 2018. Mechanisms of lysosomal positioning and movement. *Traffic*. 19:761-769.

Cardoso, C.M., L. Groth-Pedersen, M. Hoyer-Hansen, T. Kirkegaard, E. Corcelle, J.S. Andersen, M. Jaattela, and J. Nylandsted. 2009. Depletion of kinesin 5B affects lysosomal distribution and stability and induces peri-nuclear accumulation of autophagosomes in cancer cells. *PLoS One*. 4:e4424.

Cella Zanacchi, F., C. Manzo, R. Magrassi, N.D. Derr, and M. Lakadamyali. 2019. Quantifying Protein Copy Number in Super Resolution Using an Imaging-Invariant Calibration. *Biophys J*. 116:2195-2203.

Chowdhury, S., S.A. Ketcham, T.A. Schroer, and G.C. Lander. 2015. Structural organization of the dynein-dynactin complex bound to microtubules. *Nat Struct Mol Biol*. 22:345-347.

Ehmann, N., S. van de Linde, A. Alon, D. Ljaschenko, X.Z. Keung, T. Holm, A. Rings, A. DiAntonio, S. Hallermann, U. Ashery, M. Heckmann, M. Sauer, and R.J. Kittel. 2014. Quantitative super-resolution imaging of Bruchpilot distinguishes active zone states. *Nature Communications*. 5:4650.

Elshenawy, M.M., J.T. Canty, L. Oster, L.S. Ferro, Z. Zhou, S.C. Blanchard, and A. Yildiz. 2019. Cargo adaptors regulate stepping and force generation of mammalian dynein-dynactin. *Nat Chem Biol*. 15:1093-1101.

Elshenawy, M.M., E. Kusakci, S. Volz, J. Baumbach, S.L. Bullock, and A. Yildiz. 2020. Lis1 activates dynein motility by modulating its pairing with dynactin. *Nat Cell Biol*. 22:570-578.

Encalada, S.E., L. Szpankowski, C.H. Xia, and L.S. Goldstein. 2011. Stable kinesin and dynein assemblies drive the axonal transport of mammalian prion protein vesicles. *Cell*. 144:551-565.

Ferro, L.S., S. Can, M.A. Turner, M.M. ElShenawy, and A. Yildiz. 2019. Kinesin and dynein use distinct mechanisms to bypass obstacles. *Elife*. 8.

Franke, C., U. Repnik, S. Segeletz, N. Brouilly, Y. Kalaidzidis, J.M. Verbavatz, and M. Zerial. 2019. Correlative single-molecule localization microscopy and electron tomography reveals endosome nanoscale domains. *Traffic*. 20:601-617.

Friedman, J.R., J.R. Dibenedetto, M. West, A.A. Rowland, and G.K. Voeltz. 2013. Endoplasmic reticulum-endosome contact increases as endosomes traffic and mature. *Mol Biol Cell*. 24:1030-1040.

Fu, M.M., and E.L. Holzbaur. 2014. Integrated regulation of motor-driven organelle transport by scaffolding proteins. *Trends Cell Biol*. 24:564-574.

Fu, M.M., J.J. Nirschl, and E.L.F. Holzbaur. 2014. LC3 binding to the scaffolding protein JIP1 regulates processive dynein-driven transport of autophagosomes. *Dev Cell*. 29:577-590.

Gould, G.W., and J. Lippincott-Schwartz. 2009. New roles for endosomes: from vesicular carriers to multi-purpose platforms. *Nat Rev Mol Cell Biol*. 10:287-292.

Granger, E., G. McNee, V. Allan, and P. Woodman. 2014. The role of the cytoskeleton and molecular motors in endosomal dynamics. *Semin Cell Dev Biol*. 31:20-29.

Guardia, C.M., G.G. Farias, R. Jia, J. Pu, and J.S. Bonifacino. 2016. BORC Functions Upstream of Kinesins 1 and 3 to Coordinate Regional Movement of Lysosomes along Different Microtubule Tracks. *Cell Rep*. 17:1950-1961.

Hendricks, A.G., E. Perlson, J.L. Ross, H.W. Schroeder, 3rd, M. Tokito, and E.L. Holzbaur. 2010. Motor coordination via a tug-of-war mechanism drives bidirectional vesicle transport. *Curr Biol*. 20:697-702.

Hu, Y.B., E.B. Dammer, R.J. Ren, and G. Wang. 2015. The endosomal-lysosomal system: from acidification and cargo sorting to neurodegeneration. *Transl Neurodegener*. 4:18.

Hyttinen, J.M., M. Niittykoski, A. Salminen, and K. Kaarniranta. 2013. Maturation of autophagosomes and endosomes: a key role for Rab7. *Biochim Biophys Acta*. 1833:503-510.

Johansson, M., M. Lehto, K. Tanhuanpaa, T.L. Cover, and V.M. Olkkonen. 2005. The oxysterol-binding protein homologue ORP1L interacts with Rab7 and alters functional properties of late endocytic compartments. *Mol Biol Cell*. 16:5480-5492.

Johansson, M., N. Rocha, W. Zwart, I. Jordens, L. Janssen, C. Kuijl, V.M. Olkkonen, and J. Neefjes. 2007. Activation of endosomal dynein motors by stepwise assembly of Rab7-RILP-p150Glued, ORP1L, and the receptor betalll spectrin. *J Cell Biol*. 176:459-471.

Keyomarsi, K. 1996. Synchronization of mammalian cells by Lovastatin. *Methods in Cell Science*. 18:109-114.

Kimura, S., T. Noda, and T. Yoshimori. 2008. Dynein-dependent movement of autophagosomes mediates efficient encounters with lysosomes. *Cell Struct Funct*. 33:109-122.

Klumperman, J., and G. Raposo. 2014. The complex ultrastructure of the endolysosomal system. *Cold Spring Harb Perspect Biol*. 6:a016857.

Korolchuk, V.I., and D.C. Rubinsztein. 2011. Regulation of autophagy by lysosomal positioning. *Autophagy*. 7:927-928.

Korolchuk, V.I., S. Saiki, M. Lichtenberg, F.H. Siddiqi, E.A. Roberts, S. Imarisio, L. Jahreiss, S. Sarkar, M. Futter, F.M. Menzies, C.J. O'Kane, V. Deretic, and D.C. Rubinsztein. 2011. Lysosomal positioning coordinates cellular nutrient responses. *Nat Cell Biol*. 13:453-460.

Levet, F., E. Hosy, A. Kechkar, C. Butler, A. Beghin, D. Choquet, and J.B. Sibarita. 2015. SR-Tesseler: a method to segment and quantify localization-based super-resolution microscopy data. *Nat Methods*. 12:1065-1071.

Maday, S., A.E. Twelvetrees, A.J. Moughamian, and E.L. Holzbaur. 2014. Axonal transport: cargo-specific mechanisms of motility and regulation. *Neuron*. 84:292-309.

McKenney, R.J., W. Huynh, M.E. Tanenbaum, G. Bhabha, and R.D. Vale. 2014. Activation of cytoplasmic dynein motility by dynactin-cargo adapter complexes. *Science*. 345:337-341.

Mohan, N., E.M. Sorokina, I.V. Verdeny, A.S. Alvarez, and M. Lakadamyali. 2019. Detyrosinated microtubules spatially constrain lysosomes facilitating lysosome-autophagosome fusion. *J Cell Biol*. 218:632-643.

Nirschl, J.J., M.M. Magiera, J.E. Lazarus, C. Janke, and E.L. Holzbaur. 2016. alpha-Tubulin Tyrosination and CLIP-170 Phosphorylation Regulate the Initiation of Dynein-Driven Transport in Neurons. *Cell Rep*. 14:2637-2652.

Olenick, M.A., and E.L.F. Holzbaur. 2019. Dynein activators and adaptors at a glance. *J Cell Sci*. 132.

Olkkonen, V.M., and S. Li. 2013. Oxysterol-binding proteins: sterol and phosphoinositide sensors coordinating transport, signaling and metabolism. *Prog Lipid Res*. 52:529-538.

Perez-Cruz, F. 2008. Kullback-Leibler divergence estimation of continuous distributions. *In* IEEE international symposium on information theory.

Pfeffer, S.R. 2001. Rab GTPases: specifying and deciphering organelle identity and function. *Trends Cell Biol*. 11:487-491.

Pu, J., C.M. Guardia, T. Keren-Kaplan, and J.S. Bonifacino. 2016. Mechanisms and functions of lysosome positioning. *J Cell Sci*. 129:4329-4339.

Puchner, E.M., J.M. Walter, R. Kasper, B. Huang, and W.A. Lim. 2013. Counting molecules in single organelles with superresolution microscopy allows tracking of the endosome maturation trajectory. *Proc Natl Acad Sci U S A*. 110:16015-16020.

Rai, A., D. Pathak, S. Thakur, S. Singh, A.K. Dubey, and R. Mallik. 2016. Dynein Clusters into Lipid Microdomains on Phagosomes to Drive Rapid Transport toward Lysosomes. *Cell*. 164:722-734.

Reck-Peterson, S.L., W.B. Redwine, R.D. Vale, and A.P. Carter. 2018. The cytoplasmic dynein transport machinery and its many cargoes. *Nat Rev Mol Cell Biol*. 19:382-398.

Rocha, N., C. Kuijl, R. van der Kant, L. Janssen, D. Houben, H. Janssen, W. Zwart, and J. Neefjes. 2009. Cholesterol sensor ORP1L contacts the ER protein VAP to control Rab7-RILP-p150 Glued and late endosome positioning. *J Cell Biol*. 185:1209-1225.

Rosa-Ferreira, C., and S. Munro. 2011. Arl8 and SKIP act together to link lysosomes to kinesin-1. *Dev Cell*. 21:1171-1178.

Schroeder, C.M., and R.D. Vale. 2016. Assembly and activation of dynein-dynactin by the cargo adaptor protein Hook3. *J Cell Biol*. 214:309-318.

Soppina, V., A.K. Rai, A.J. Ramaiya, P. Barak, and R. Mallik. 2009. Tug-of-war between dissimilar teams of microtubule motors regulates transport and fission of endosomes. *Proc Natl Acad Sci U S A*. 106:19381-19386.

Tanemura, M. 2003. Statistical distributions of Poisson Voronoi cells in two and three dimensions. *FORMA-TOKYO*. 18:221-247.

Torres, S., E. Balboa, S. Zanlungo, C. Enrich, C. Garcia-Ruiz, and J.C. Fernandez-Checa. 2017. Lysosomal and Mitochondrial Liaisons in Niemann-Pick Disease. *Front Physiol*. 8:982.

Urnavicius, L., C.K. Lau, M.M. Elshenawy, E. Morales-Rios, C. Motz, A. Yildiz, and A.P. Carter. 2018. Cryo-EM shows how dynactin recruits two dyneins for faster movement. *Nature*. 554:202-206.

van der Kant, R., I. Zondervan, L. Janssen, and J. Neefjes. 2013. Cholesterol-binding molecules MLN64 and ORP1L mark distinct late endosomes with transporters ABCA3 and NPC1. *J Lipid Res*. 54:2153-2165.

Vanlandingham, P.A., and B.P. Ceresa. 2009. Rab7 regulates late endocytic trafficking downstream of multivesicular body biogenesis and cargo sequestration. *J Biol Chem*. 284:12110-12124.

Verdeny-Vilanova, I., F. Wehnekamp, N. Mohan, A. Sandoval Alvarez, J.S. Borbely, J.J. Otterstrom, D.C. Lamb, and M. Lakadamyali. 2017. 3D motion of vesicles along microtubules helps them to circumvent obstacles in cells. *J Cell Sci*. 130:1904-1916.

Vihervaara, T., R.L. Uronen, G. Wohlfahrt, I. Bjorkhem, E. Ikonen, and V.M. Olkkonen. 2011. Sterol binding by OSBP-related protein 1L regulates late endosome motility and function. *Cell Mol Life Sci*. 68:537-551.

Wijdeven, R.H., H. Janssen, L. Nahidiazar, L. Janssen, K. Jalink, I. Berlin, and J. Neefjes. 2016. Cholesterol and ORP1L-mediated ER contact sites control autophagosome transport and fusion with the endocytic pathway. *Nat Commun*. 7:11808.

Zanacchi, F.C., C. Manzo, A.S. Alvarez, N.D. Derr, M.F. Garcia-Parajo, and M. Lakadamyali. 2017a. A DNA origami platform for quantifying protein copy number in super-resolution. *Nat Methods*. 14:789-792.

Zanacchi, F.C., C. Manzo, A.S. Alvarez, N.D. Derr, M.F. Garcia-Parajo, and M. Lakadamyali. 2017b. A DNA origami platform for quantifying protein copy number in super-resolution. *Nature Methods*. 14:789-792.

Zhao, K., and N.D. Ridgway. 2017. Oxysterol-Binding Protein-Related Protein 1L Regulates Cholesterol Egress from the Endo-Lysosomal System. *Cell Rep*. 19:1807-1818.

Figures:

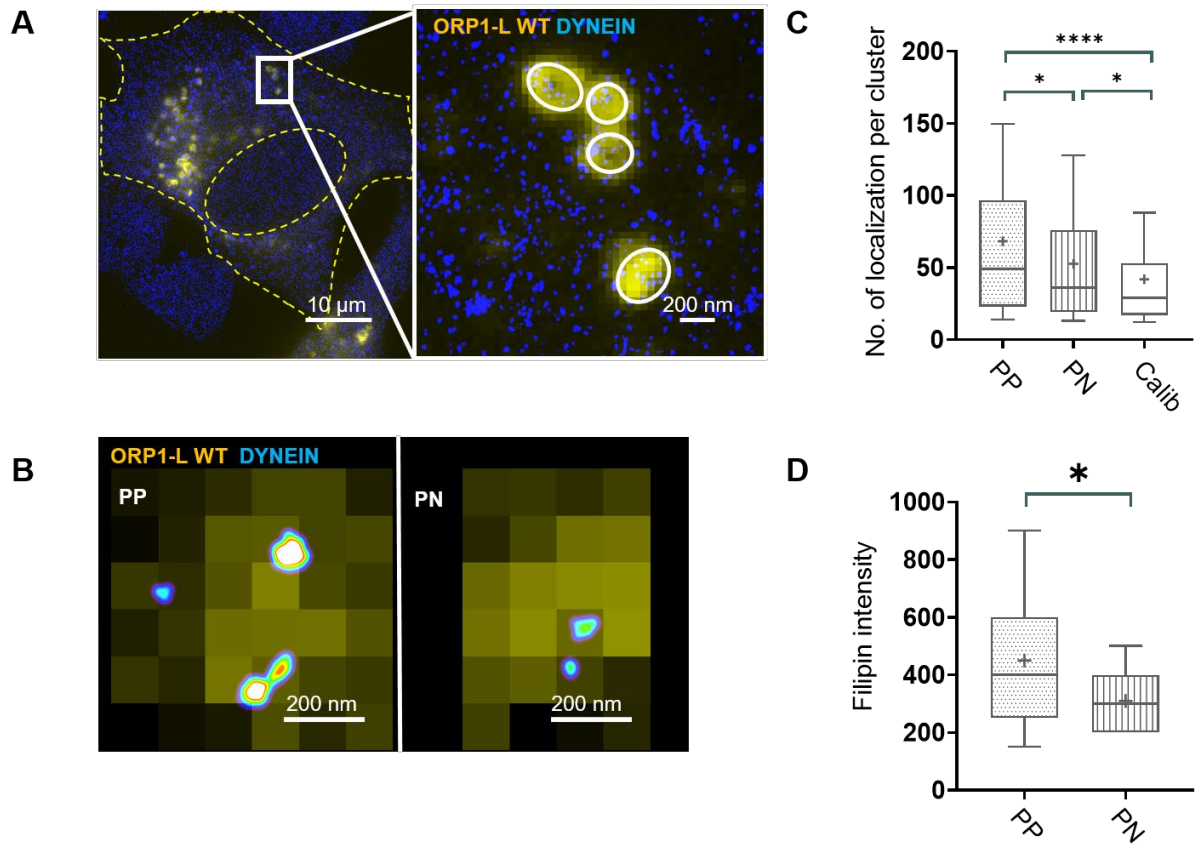

Figure 1: Dynein forms larger nano-clusters containing a higher proportion of dynein multimers on endolysosomes positioned at the cell periphery:

(A) Cropped wide-field image of cells expressing full length ORP1L fused to mCherry (mCherry-ORP1L-WT, yellow) overlaid with super-resolution image of dynein (blue). Cell edge and nucleus are highlighted in yellow dashed lines. A zoom of the white rectangle is shown in which mCherry-ORP1L-WT positive endolysosomes are highlighted with white circles.

(B) An overlay of wide-field image of ORP1L (yellow) and super-resolution image of dynein (image is color coded according to localization density with higher density corresponding to white and lower density corresponding to cyan) for an endolysosome positioned at the cell periphery (PP) and peri-nuclear region (PN).

(C) Box plot showing the number of localizations per dynein nano-cluster for peripherally positioned endolysosomes (PP) (n=195 endolysosomes from n=6 cells, n=2experiments), peri-nuclearly positioned endolysosomes (PN) (n=210 endolysosomes from n=6 cells, n=2 experiments) and in cells in which dynein has been labeled with a 100-fold dilution of the primary antibody for sparsely labeling single dynein motors (n=6 cells, n=1 experiments). The box corresponds to 25-75 percentile, the line corresponds to the median, the cross corresponds to the mean, and the whiskers correspond to 10-90 percentile. Statistical significance was assessed using a Kolmogorov-Smirnov-test with a p-value of 0.012.

(D) Box plot showing the intensity of filipin, which binds cholesterol, on peripherally positioned endolysosomes (PP) (n=50 endolysosomes from n=4 cells, n=2 experiments) versus peri-nuclearly positioned endolysosomes (PN) (n=80 endolysosomes from n=5 cells, n=2 experiments). The box corresponds to 25-75 percentile, the line corresponds to the median, the cross corresponds to the mean and the whiskers correspond to 10-90 percentile. Statistical significance was assessed using an unpaired t-test with a p-value of 0.011

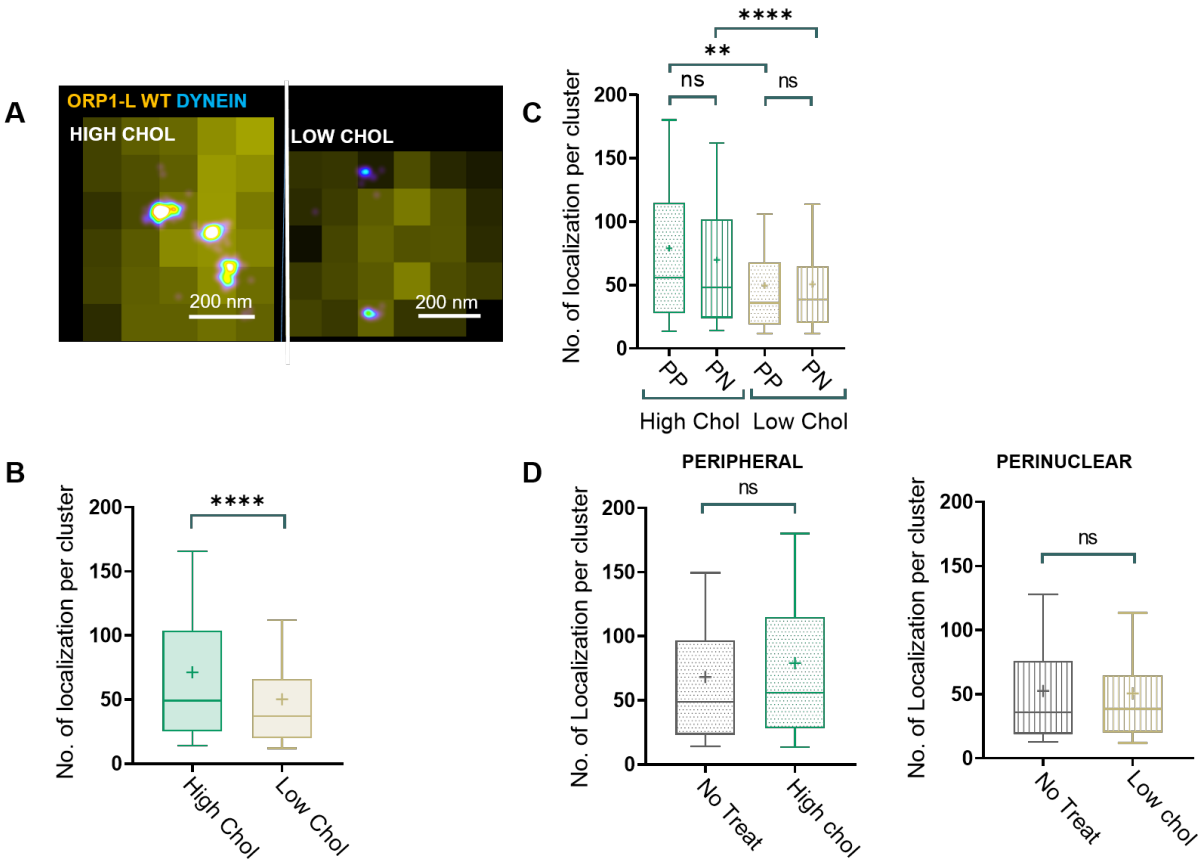

Figure 2: Dynein forms larger nano-clusters containing a higher proportion of dynein multimers on endolysosomes that have high cholesterol content compared to those that have low cholesterol content:

(A) An overlay of cropped wide-field image of ORP1L (yellow) and super-resolution image of dynein (image is color coded according to localization density with higher density corresponding to white and lower density corresponding to cyan) for an endolysosome in cells treated with U18666A (High Chol) or Lovastatin (Low Chol).

(B) Box plot showing the number of localizations per dynein nano-cluster for endolysosomes in U18666A treated cells (High Chol) (n=224 endolysosomes from n=6 cells, n=2 experiments) versus Lovastatin treated cells (Low Chol) (n=217 endolysosomes from n=6 cells, n=2 experiments). The box corresponds to 25-75 percentile, the line corresponds to the median, the cross corresponds to the mean and the whiskers correspond to 10-90 percentile. Statistical significance was assessed using a Kolmogorov-Smirnov-test with a p-value <0.0001.

(C) Box plot showing the number of localizations per dynein nano-cluster for peripherally positioned (n=70 endolysosomes from n=6 cells, n=2 experiments) or perinuclearly positioned (n=154 endolysosomes from n=6 cells, n=2 experiments) endolysosomes in U18666A treated cells (High Chol PP and High Chol PN, respectively) or Lovastatin treated cells (Low Chol PP; n=110endolysosomes from n=6 cells, n=2 experiments and Low Chol PN; n=107 endolysosomes from n=6 cells, n=2 experiments, respectively). The box corresponds to 25-75 percentile, the line corresponds to the median, the cross corresponds to the mean and the whiskers correspond to 10-90 percentile. Statistical significance was assessed using a Kolmogorov-Smirnov-test with a p-value of n.s.: 0.27, n.s.: 0.93, **: 0.001, ****: <0.0001.

(D) Box plot showing the number of localizations per dynein nano-cluster for peripherally positioned endolysosomes in untreated cells (No Treat) (n=195 endolysosomes from n=6 cells, n=2 experiments) and U18666A treated cells (High Chol) (n=70 endolysosomes from n=6 cells, n=2 experiments); as well as in perinuclearly positioned endolysosomes in untreated cells (No Treat) (n=210 endolysosomes from n=6 cells, n=2 experiments) and Lovastatin treated cells (Low Chol) (n=107 endolysosomes from n=6 cells, n=2 experiments). The box corresponds to 25-75 percentile, the line corresponds to the median, the cross corresponds to the mean and the whiskers correspond to 10-90 percentile. Statistical significance was assessed using a Kolmogorov-Smirnov-test with a p-value of 0.23 and 0.7.

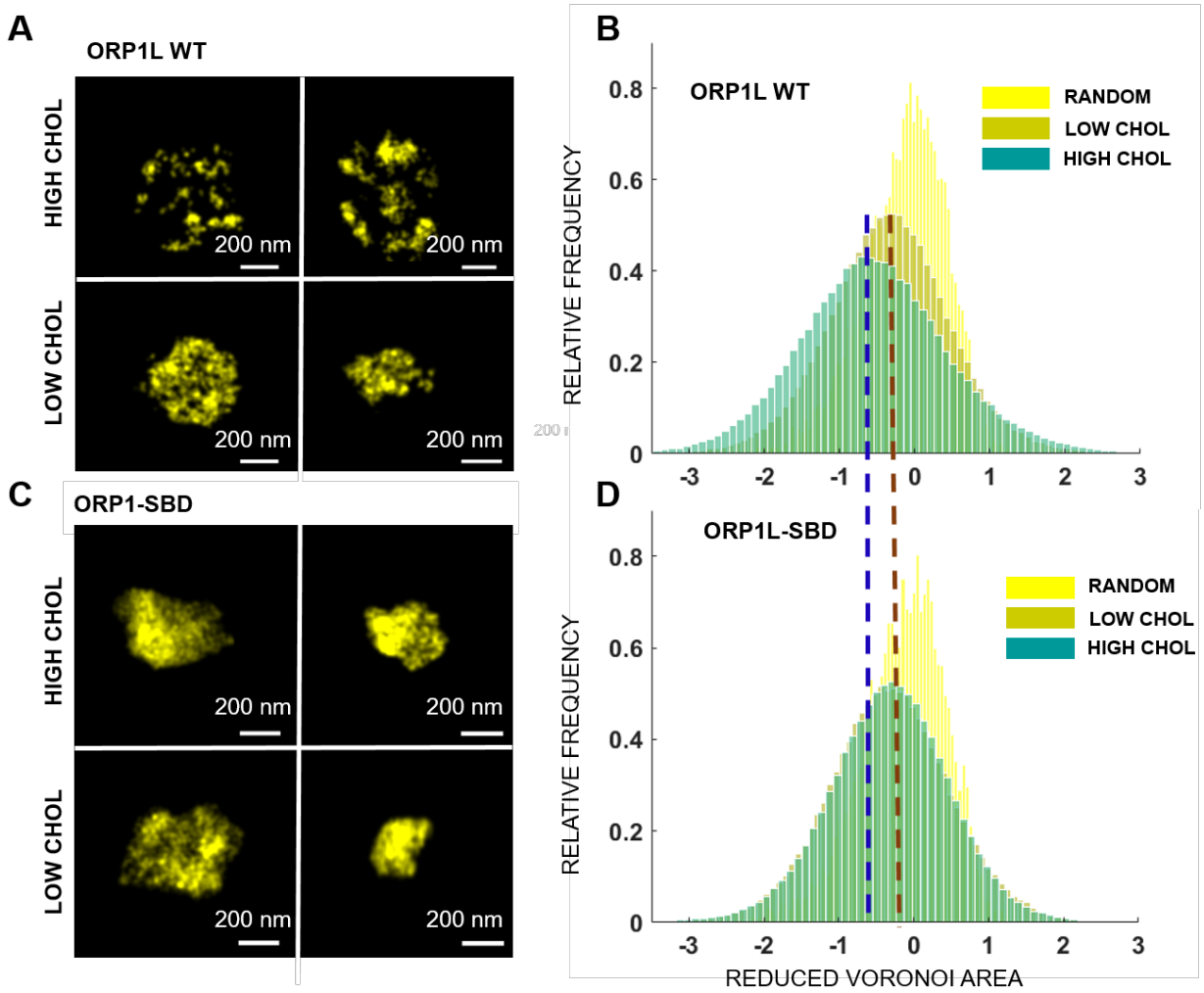

Figure 3: ORP1L is more clustered on endolysosomes having higher cholesterol levels in a manner dependent on its cholesterol binding domain:

(A) Super-resolution images of full length ORP1L (mCherry-ORP1L-WT) in cells treated with U18666A (High Chol, upper panels) and in cells treated with Lovastatin (Low Chol, lower panels).

(B) Log plot of the Reduced Voronoi Polygon area distribution for super-resolution images of full length ORP1L (mCherry-ORP1L-WT) in cells treated with U18666A (dark green, High Chol) (n=110 endolysosomes from n=6 cells, n=2 experiments), Lovastatin (light green, Low Chol) (n=120 endolysosomes from n=6 cells, n=2 experiments) and for a random distribution of localizations (yellow, Random). The dashed lines are a guide to the eye to highlight the shift in the peak position of Reduced Voronoi Polygon area distributions with

cholesterol treatment for full length ORP1L (mCherry-ORP1L-WT) and sterol binding deficient ORP1L mutant lacking residues 560-563 (mCherry-ORP1L-SBD).

(C) Super-resolution images of sterol binding deficient ORP1L mutant lacking residues 560-563 (mCherry-ORP1L-SBD) in cells treated with U18666A (High Chol, upper panels) and in cells treated with Lovastatin (Low Chol, lower panels).

(D) Log plot of the Reduced Voronoi Polygon area distribution for super-resolution images of sterol binding deficient ORP1L mutant lacking residues 560-563 (mCherry-ORP1L-SBD) in cells treated with U18666A (dark green, High Chol) (n=120 endolysosomes from n=6 cells, n=2 experiments), Lovastatin (light green, Low Chol) (n=170 endolysosomes from n=6 cells, n=2 experiments) and for a random distribution of localizations (yellow, Random).

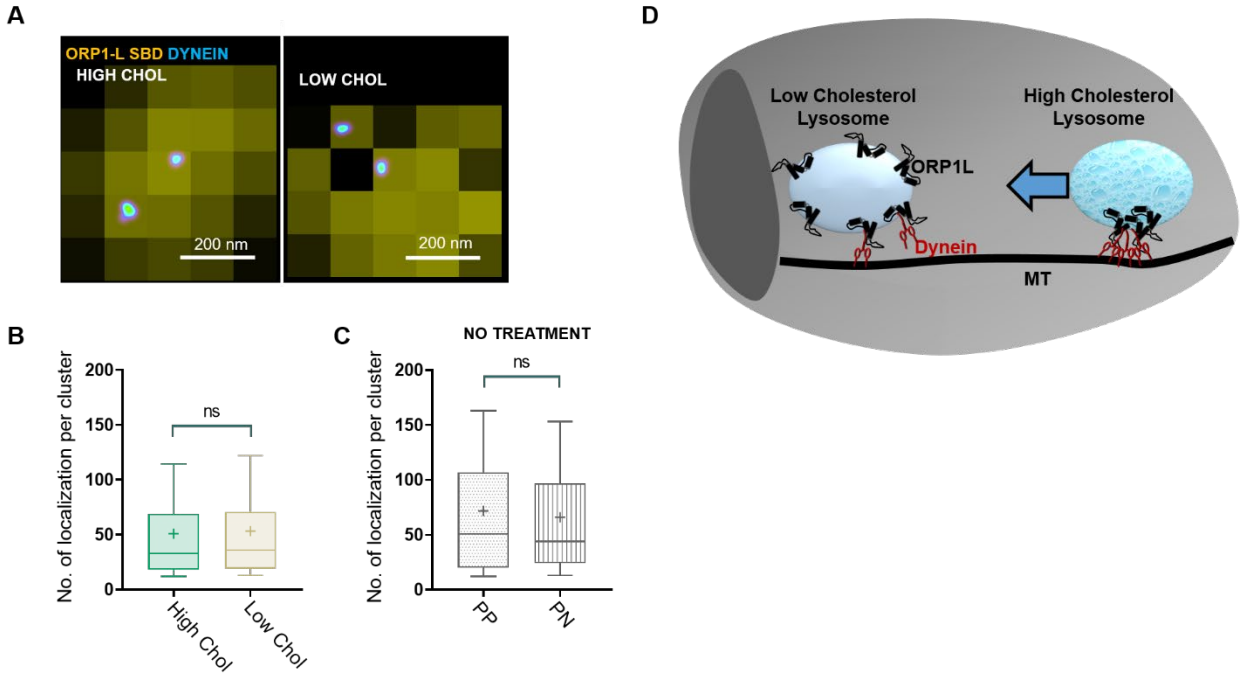

Figure 4: Dynein nano-clusters are insensitive to cholesterol levels in cells expressing sterol binding deficient ORP1L mutant:

(A) An overlay of cropped wide-field image of ORP1L (yellow) and super-resolution image of dynein (image is color coded according to localization density with higher density corresponding to white and lower density corresponding to cyan) for an endolysosome in

cells expressing sterol binding deficient ORP1L mutant lacking residues 560-563 (mCherry-ORP1L-SBD) and treated with U18666A (High Chol) or Lovastatin (Low Chol).

(B) Box plot showing the number of localizations per dynein nano-cluster for endolysosomes in cells expressing the sterol binding deficient ORP1L mutant lacking residues 560-563 (mCherry-ORP1L-SBD) and treated with U18666A (High Chol) (n=450 endolysosomes from n=6 cells, n=2 experiments) versus Lovastatin (Low Chol) (n=300 endolysosomes from n=6 cells, n=2 experiments). The box corresponds to 25-75 percentile, the line corresponds to the median, the cross corresponds to the mean and the whiskers correspond to 10-90 percentile. Statistical significance was assessed using a Kolmogorov-Smirnov-test with a p-value of 0.06.

(C) Box plot showing the number of localizations per dynein nano-cluster for peripherally positioned endolysosomes (n=100 endolysosomes from n=5 cells, n=2 experiments) and peri-nuclearly positioned endolysosomes (n=150 endolysosomes from n=5 cells, n=2 experiments) in cells expressing the sterol binding deficient ORP1L mutant lacking residues 560-563 (mCherry-ORP1L-SBD). The box corresponds to 25-75 percentile, the line corresponds to the median, the cross corresponds to the mean and the whiskers correspond to 10-90 percentile. Statistical significance was assessed using a Kolmogorov-Smirnov-test with a p-value of 0.44.

(D) Cartoon model showing how cholesterol levels and ORP1L regulate dynein nano-clustering and endolysosome positioning. Peripheral lysosomes with higher cholesterol content have a more clustered organization of ORP1L and dynein leading to efficient retrograde transport (blue arrow). Perinuclear lysosomes having lower cholesterol content have more uniform ORP1L organization leading to lower dynein recruitment and clustering likely facilitating endolysosome anchoring at the peri-nuclear region or anterograde trafficking back to the cell periphery.